

# A humidity dose-CZM formulation to simulate new end-of-life recycling methods for photovoltaic laminates

Z. Liu<sup>a,b,\*</sup>, J. Reinoso<sup>b</sup>, M. Paggi<sup>a</sup>

<sup>a</sup> *IMT School for Advanced Studies Lucca, Piazza San Francesco 19, 55100, Lucca, Italy*

<sup>b</sup> *Elasticity and Strength of Materials Group, School of Engineering, University of Seville, Camino de los Descubrimientos s/n, 41092, Seville, Spain*

## ARTICLE INFO

### Keywords:

Cohesive zone model  
Adhesion strength  
Humidity dose model  
Photovoltaics recycling

## ABSTRACT

Humidity and temperature greatly influence the degradation of interfacial adhesion in photovoltaic (PV) modules. Besides, for an accurate prediction of the required energy to peel off the different plies of end-of-life PV laminates for recycling purposes, it is also essential to take these factors into account. A polynomial cohesive zone model (CZM) coupled with a humidity dose model is herein proposed to address these issues in the finite element (FE) framework. A novel three-dimensional interface finite element considering large deformation is adopted to accurately deal with the coupled material and geometrical nonlinearities involved in peeling tests. A consistent derivation and operator formulations for this interface finite element are detailed. Consistency between numerical predictions and peeling experimental results taken from the literature confirms the validity of the proposed approach. From the technical viewpoint, the numerical results show that peeling is energetically preferable over crushing to disassemble and recycle PV laminates at the end of their lifetime. The proposed modeling approach can effectively contribute to virtually design new methods for PV recycling.

## 1. Introduction

The vast majority of PV modules consists in laminates composed of tempered glass, solar cells, backsheet and encapsulant layers, see Fig. 1. Different components are adhesively bonded to each other. This multilayer system can ensure the safety and performance of PV modules but forms a number of interfaces that are potential paths for contaminant ingress, and causing subsequent delamination events [1,2]. This issue eventually promotes many other further ageing mechanisms such as polymer degradation, corrosion of metallic materials inside the system, loss of light transmission, and so on [3,4]. The reliability of encapsulation is therefore crucial for the durability and the service life of PV modules [5,6]. The most commonly used encapsulant material in the existing PV installations is Epoxy Vinyl Acetate (EVA) that, interposed in the form of layers between the glass and the silicon solar cells, and between the solar cells and the backsheet, holds the components together and protects the module from outside harsh environments [7]. It has been shown by field inspection that encapsulant-related degradation is one of the most critical failure modes in PV systems [8].

The adhesion strength of the material interfaces in PV modules is greatly influenced by the operating environment, depending on different factors, including humidity, temperature, and irradiance [9,10]. Moisture weakens the ionic attraction of the bond and physical adsorption across the interface due to the high permittivity of water, which is highly relevant to the properties of high polarity adherend [11]. Both the ionic attraction force and van der Waals forces are inversely proportional to the relative

\* Corresponding author at: IMT School for Advanced Studies Lucca, Piazza San Francesco 19, 55100, Lucca, Italy.  
E-mail address: [zeng.liu@imtlucca.it](mailto:zeng.liu@imtlucca.it) (Z. Liu).

**Nomenclature**

$\delta$	ultimate displacement
$\delta II_{\text{intf}}$	virtual work contribution of the interface
$\delta_0$	initial ultimate displacement corresponding to no damp-heat effect
$\lambda$	dimensionless displacement
$\mathbf{F}_v$	volume force
$\mathbf{t}^i, \mathbf{u}^i$	force and displacement boundary conditions
$B_0, S_0$	deformable body and interface
$\mu$	difference factor between tangential and normal separation
$\sigma_{\text{max}}$	maximum stress
$\mathbf{C}$	tangent constitutive matrix
$\mathbf{d}$	nodal displacement vector
$\mathbf{F}$	deformation gradient
$\mathbf{f}_{\text{int}}^e$	internal force vector of interface at the element level
$\mathbf{g}_{\text{loc}}$	displacement gap vector
$\mathbf{K}^e$	element stiffness
$\mathbf{K}_{\text{geom}}^e$	element geometrical stiffness
$\mathbf{K}_{\text{mat}}^e$	element material stiffness
$\mathbf{L}$	difference operator
$\mathbf{M}$	averaging operator
$\mathbf{N}$	shape function operator
$\mathbf{R}$	rotation operator
$\mathbf{s}, \mathbf{t}, \mathbf{n}$	convective shear, tangential and normal vector
$\mathbf{T}$	traction vector
$\mathbf{u}$	displacement vector
$\mathbf{X}, \mathbf{x}$	material position vectors in the reference and current configuration
$\mathbf{X}^n, \mathbf{x}^n$	nodal material position vectors in the reference and current configurations
$E_a$	activation energy
$g_{\text{loc},n}$	normal gap vector component
$g_{\text{loc},s}$	in-plane shear gap vector component
$g_{\text{loc},t}$	out-plane shear gap vector component
$J$	Jacobian
$R$	Boltzmann's constant
$dose$	humidity dose
$f$	enhancement coefficient
$P_s$	saturated water vapor pressure
$P_w$	water vapor pressure of the environment
$RH_a$	ambient relative humidity
$RH_m$	module relative humidity
$T_a$	ambient temperature
$T_m$	module temperature

permittivity, and a small amount of water will significantly reduce the adhesion strength [12]. Besides, the high surface tension resulting from the high polarity of water reduces the thermodynamic work of adhesion and thus damage interface durability [13]. Temperature mechanically affects the performance of PV modules through differential thermal expansion, as can be seen in real life because of daily and seasonal thermal cycles. However, it is assumed that the loss of adhesion strength is primarily reduced by moisture ingress, and temperature acts as an accelerator of the effects of humidity [14,15].

Taking into consideration the previous discussion, this research aims at understanding the influence of moisture penetration accelerated by temperature on the adhesion durability of interfaces in the PV system. More specifically, the target is to develop a computational framework allowing for the accurate simulation of delamination in PV modules for different ageing conditions. In this regard, the current research is motivated by the fact that peeling techniques could be exploited to partially disassemble PV laminates at the end of their lifetime. This can be energetically and economically favorable over the actual recycling operations which consider a full crushing of the glass laminate and then separation of its recyclable components afterwards.

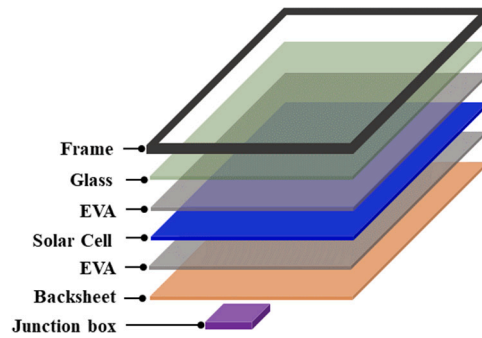


Fig. 1. General structure of a photovoltaic module.

From a mechanical perspective in terms of modelling fracture phenomena, during the past decades, cohesive zone models (CZM) have been widely incorporated into the nonlinear finite element method for engineering applications concerning the formation of free surfaces due to fracture [16]. In comparison to alternative methods such as the virtual crack closure technique (VCCT) [17], CZM can be easily implemented into research and commercial codes and is highly versatile to accommodate different physical phenomena. CZM is a nonlinear traction–relative displacement relationship between the interface tractions across the discontinuity and the sliding and opening displacements. Applications cover many fields, such as quasi-static fracture in solids [18,19], snap-back instabilities during crack propagation [20,21], crack propagation in composites [22–24], micromechanical and multiscale analyses [25,26], and crack assessment in bio-inspired materials [27], among others. However, to the best knowledge of the authors, no previous research considers effect of environmental factors including both moisture and temperature on the interfacial strength in CZM for numerical prediction of fracture especially towards PV lifetime recycling.

Peeling of layers of the laminate from the layer of solar cells would require large deformation simulations [28], since the deformed configuration cannot be approximated by the undeformed one. As a result, the interfacial gap calculated according to the initial undeformed configuration can result in errors that cannot be ignored when assessing the total energy required for peeling, which is the quantity of primary interest for recycling. In order to accurately accommodate the large deformation framework in CZMs, both the surface separation and relative rotation between two sides of the interface need to be taken into account. A first attempt has been proposed in [29], which adopted the middle surface of the cohesive element in the deformed configuration as the reference plane to update the calculation of the normal and tangential directions of the interface. Nevertheless, this formulation stemming from differentiation of cohesive tractions with regard to normal unit vector led to a non-symmetric geometric stiffness matrix. Based on that research, a 3D interface finite element was used to simulate fracture mechanics tests in thin aluminum panels, in which the residual vector with rotation matrix is updated during the deformation process [30]. However, its linearization did not consider the dependence of differential operator with respect to the kinematic field. An alternative formulation for a large displacement interface finite element was proposed in [31] by introducing a co-rotational reference system coincident with one of the deformed surfaces of the interface element, which might present notable difficulties for its implementation into the finite element method due to this co-rotational description. In order to account for large deformation of the interface, the latest version of the interface finite element formulation for both geometrical and material nonlinearities developed in [32] is herein adopted and herein extended to 3D applications.

Particularly, in this study, the polynomial CZM [33] coupled with strength degradation by the humidity dose model [14] is proposed for the first time. Then, it is incorporated into the 3D large deformation interface finite element extended from the 2D version proposed in [32]. The numerical results obtained from this coupling strategy is compared with experimental results [14] exhibiting a very satisfactory correlation in terms of adhesion strength between backsheets and encapsulant layers in PV. Finally, the difference between the specific energy required in peeling and traditional crushing for recycling of PV panels is compared and discussed, and it is concluded that this modeling approach can be very promising for recycling application in PV industry.

## 2. Humidity dose-based cohesive zone model

In this section, the humidity dose concept integrated into the polynomial CZM for the accurate simulation of the hygrothermal-mechanical behavior of the EVA adhesive layer, subject to large deformation like peeling, is presented. The formulations described subsequently are macroscopic models and developed for use within the framework of the finite element method.

### 2.1. Humidity dose model

Adhesion strength of EVA encapsulant within the PV module under different environmental conditions degrades similarly in the form of exponential decay, which tends to decrease quickly in the beginning and then it slows down after a certain period. Increased moisture causes the loss of interfacial strength, while temperature enhances the effect of humidity at a faster speed. In order to describe the environmental impact on the module over a time period, the relative humidity under ambient temperature must

be transformed into the relative humidity in the module encapsulant. The relative humidity inside the module is usually lower than the ambient relative humidity. Assuming the EVA interface is in thermodynamic equilibrium with the environment and temperature inside the PV module is uniform [34], the ambient and module relative humidity can be calculated as

$$RH_a = \frac{P_w}{P_s(T_a)} \quad (1a)$$

$$RH_m = \frac{P_w}{P_s(T_m)} = \frac{RH_a \times P_s(T_a)}{P_s(T_m)} \quad (1b)$$

where  $RH_a$  and  $RH_m$  are the ambient and module relative humidity, respectively,  $P_w$  is the water vapor pressure of the environment, and  $P_s(T_a)$  and  $P_s(T_m)$  are, respectively, the saturated water vapor pressures at ambient temperature and the module temperature. The saturated and partial water vapor pressure of the environment are calculated as

$$P_s = f \times P'_s \quad (2a)$$

$$P_w = RH_a \times P_s = RH_a \times f \times P'_s \quad (2b)$$

where  $P_s$  and  $P'_s$  are the saturated water vapor pressure of environment and pure value, respectively, and  $f$  is an enhancement coefficient. Substituting Eqs. (2a) and (2b) into Eq. (1b), the module relative humidity is formulated as

$$RH_m = \frac{P_w}{P_s(T_m)} = \frac{RH_a \times f(T_a) \times P'_s(T_a)}{f(T_m) \times P'_s(T_m)} \quad (3)$$

where  $P'_s(T_a)$  and  $P'_s(T_m)$  are pure saturation water vapor pressure at ambient temperature  $T_a$  and module temperature  $T_m$ , and  $f(T_a)$  and  $f(T_m)$  are enhancement coefficients at corresponding temperatures, respectively. Due to many different environmental factors such as irradiance, wind speed, heat exchange, and so on, module temperature is usually different from ambient temperature for outdoor exposure. However, for a standard laboratory damp-heat test, the module temperature is very close to the ambient temperature, as experiments are performed in the environmental chambers. Major differences need to be taken into account for the prediction of outdoor installation or for accelerated cyclic tests with fast non-equilibrium temperature variations.

The humidity dose model is established to quantify the environmental humidity and temperature effect on the interfacial degradation of PV modules within a certain time duration. In this model, the relative humidity is regarded as the dominating factor, while the temperature is an accelerating factor, which can be described by an Arrhenius function. This Arrhenius form is an acceleration formulation to define relationships between degradation and contributing factors when a single mechanism dominates the influence [35], allowing a consistent model for different operating environments to be established. The humidity dose can be defined as a function of relative surface humidity with temperature as weighting factor within the time duration

$$dose = RH_m \times e^{-\frac{E_a}{RT_m}} \times \Delta t \quad (4)$$

where  $R$  is Boltzmann's constant ( $8.617 \times 10^{-5}$  eV/K),  $E_a$  is the activation energy and  $T_m$  is the module temperature in Kelvin (K). Considering the relative module humidity defined in Eq. (3), the humidity dose can be formulated as follows,

$$dose = \frac{RH_a \times f(T_a) \times P'_s(T_a)}{f(T_m) \times P'_s(T_m)} \times e^{-\frac{E_a}{RT_m}} \times \Delta t \quad (5)$$

This means the relative humidity of the PV module rather than the ambient relative humidity determines the moisture ingress. Besides, it also considers the temperature effect on moisture diffusion. The critical parameter in this dose model for the prediction of ageing is the activation energy, which is determined as 0.65 eV by curve fitting [14].

## 2.2. Polynomial CZM coupled with moisture and temperature effects

Polynomial CZM proposed by Tvergaard [33] is a nonlinear constitutive relationship where the traction vector  $\mathbf{T} = (\tau_s, \tau_t, \sigma)^T$  is defined as a function of opening and sliding displacement measures of an interface with a decaying part after reaching the maximum tractions. In this model, a non-dimensional parameter  $\lambda$  is firstly defined as

$$\lambda = \sqrt{\left(\frac{g_{loc,s}}{\delta}\right)^2 + \left(\frac{g_{loc,t}}{\delta}\right)^2 + \left(\frac{g_{loc,n}}{\delta}\right)^2} \quad (6)$$

where  $g_{loc,n}$ ,  $g_{loc,s}$  and  $g_{loc,t}$  are normal, in-plane shearing and out-of-plane shearing gap vector components, and  $\delta$  is the corresponding ultimate displacement. In this research, the shearing ultimate displacement values are set the same as the normal displacement one. Complete separation occurs when reaching the ultimate dimensionless displacement  $\lambda = 1$ . An exponential model can be used to describe the relation between ultimate displacement  $\delta$  and humidity dose during degradation,

$$\delta = \delta_0 e^{-k \times dose} \quad (7)$$

where  $k$  is the coefficient determined as  $3.28 \times 10^7$  [14], and  $\delta_0$  is the initial ultimate displacement corresponding to no damp-heat effect, which is quantified as 15 mm by the trial simulation to match experimental results without ageing effects.

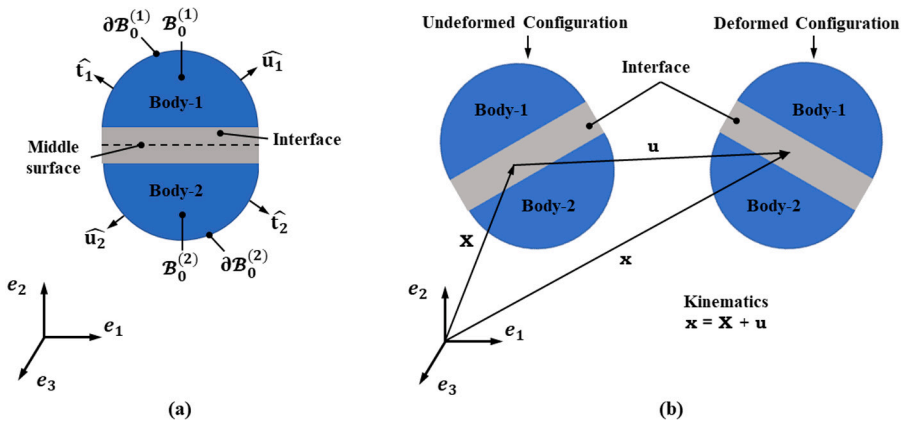


Fig. 2. A sketch of schematic and kinematic definitions of the interface between two bodies along the deformation process.

In order to define the interface constitutive behavior in a consistent manner, a polynomial function is defined as

$$P(\lambda) = \frac{27}{4} \sigma_{\max} (1 - 2\lambda + \lambda^2) \quad \text{for } 0 \leq \lambda \leq 1 \quad (8)$$

where  $\sigma_{\max}$  is the maximum stress, which is defined by trial simulation and specified as a constant value of 0.3 MPa throughout this study for all the cases. Then, the traction components are given by the following expressions

$$\sigma = \sigma_{\max} \frac{g_{\text{loc},n}}{\delta} P(\lambda) \quad (9a)$$

$$\tau_s = \mu \sigma_{\max} \frac{g_{\text{loc},s}}{\delta} P(\lambda) \quad (9b)$$

$$\tau_t = \mu \sigma_{\max} \frac{g_{\text{loc},t}}{\delta} P(\lambda) \quad (9c)$$

where  $\mu$  is the difference factor between tangential and normal separation, and set as 0.1 in this work. This cohesive zone formulation is viewed as a phenomenological model representing the average effect of the debonding mechanisms of PV interfaces.

The tangent constitutive matrix of the current interface model reads as

$$\mathbf{C} = \begin{bmatrix} \frac{\partial \tau_s}{\partial g_{\text{loc},s}} & \frac{\partial \tau_s}{\partial g_{\text{loc},t}} & \frac{\partial \tau_s}{\partial g_{\text{loc},n}} \\ \frac{\partial \tau_t}{\partial g_{\text{loc},s}} & \frac{\partial \tau_t}{\partial g_{\text{loc},t}} & \frac{\partial \tau_t}{\partial g_{\text{loc},n}} \\ \frac{\partial \sigma}{\partial g_{\text{loc},s}} & \frac{\partial \sigma}{\partial g_{\text{loc},t}} & \frac{\partial \sigma}{\partial g_{\text{loc},n}} \end{bmatrix} \quad (10)$$

### 3. 3D Large deformation interface element and FE implementation

#### 3.1. Variational form of interface element

In the reference configuration for finite deformation setting, let consider two deformable bodies  $B_0^{(1)} \subset \mathbb{R}^n$  and  $B_0^{(2)} \subset \mathbb{R}^n$  (identified as Body-1 and Body-2 in Fig. 2(a), where  $n = 3$  stands for the space dimension). Both the boundary conditions:  $\mathbf{t}^i = \hat{\mathbf{t}}_i$  on  $\partial B_{0,t}^{(i)}$  and  $\mathbf{u}^i = \hat{\mathbf{u}}_i$  on  $\partial B_{0,u}^{(i)}$  and volume forces  $\mathbf{F}_v^{(i)}$  with  $i = 1, 2$  are imposed on the two separate bodies. It is worth mentioning that two bodies can obey different constitutive material laws that characterize the mechanical performance within their domain. A deformation map  $\varphi(\mathbf{X}) : \mathbf{X} \rightarrow \mathbf{x}$  is defined to relate material point in the reference configuration  $\mathbf{X} \in B_0^{(i)}$  to the corresponding point in the deformed configuration  $\mathbf{x} \in B_t^{(i)}$  at time  $t$ , see Fig. 2(b).

In order to determine the linear map between the reference and deformed configuration, the deformation gradient of transformation is defined as:  $\mathbf{F} := \partial_{\mathbf{X}} \varphi(\mathbf{x}, t)$  where  $\partial_{\mathbf{X}}$  denotes the partial derivative with respect to the reference configuration. Jacobian can then be defined as the determinant of deformation gradient, which can be expressed as  $J = \det[\mathbf{F}] > 0$ . Noted that interface between two bodies  $S_0 \subset \mathbb{R}^{n-1}$  is characterized by the polynomial cohesive zone formulation coupling with humidity dose model described in Section 2 for 3D applications.

Focusing on the analysis of the interface between the two bodies, its contribution to the Principle of Virtual Work of the whole mechanical system can be expressed as

$$\Pi_{\text{intr}}(\mathbf{g}_{\text{loc}}) = \int_{S_0} \mathbf{g}_{\text{loc}}^T \mathbf{T} dS \quad (11)$$

where  $\mathbf{g}_{\text{loc}} = (g_{\text{loc},s}, g_{\text{loc},t}, g_{\text{loc},n})^T$  is the displacement gap vector including both opening and sliding components between the two opposite sides of an interface, and  $\mathbf{T}$  is the traction vector conjugated to the gap vector. Note that the traction vector

defined previously is the Piola–Kirchhoff stress defined in the reference configuration due to the geometrical nonlinearity. In a large deformation setting, the traction vector vanishes when the interface is undergoing rigid body motions owing to the frame indifference of this formulation. The variational form of interface contribution on the basis of the Principle of Virtual Work is expressed as

$$\delta H_{\text{intf}}(\mathbf{g}_{\text{loc}}) = \int_{S_0} \left( \frac{\partial \mathbf{g}_{\text{loc}}}{\partial \mathbf{u}} \delta \mathbf{u} \right)^T \mathbf{T} \, dS = \delta \mathbf{u}^T \int_{S_0} \left( \frac{\partial \mathbf{g}_{\text{loc}}}{\partial \mathbf{u}} \right)^T \mathbf{T} \, dS \quad (12)$$

In the case of large deformation, the position vector in the deformed configuration can be calculated as  $\mathbf{x} = \mathbf{X} + \mathbf{u}$ , see Fig. 2(b). To account for moderate rotations, it is convenient to define a middle plane of the interface by averaging the position and displacement vector of the upper and lower faces in the deformed configuration. Hence, the position vector for any material point vector on the middle surface  $\bar{\mathbf{x}}$  can be determined by multiplying the position vector with an averaging operator  $\mathbf{M}$  (which is defined subsequently):

$$\bar{\mathbf{x}} = \mathbf{M}\mathbf{x} \quad (13)$$

### 3.2. FE formulation

Complying with the isoparametric concept, the discrete version of the position vector  $\bar{\mathbf{x}}^e$  and  $\bar{\mathbf{X}}^e$  can be obtained by the operator  $\mathbf{N}$  that collects the shape functions,

$$\bar{\mathbf{x}}^e = \mathbf{N}\mathbf{M}\mathbf{x}^n, \quad \bar{\mathbf{X}}^e = \mathbf{N}\mathbf{M}\mathbf{X}^n \quad (14)$$

where  $\mathbf{x}^n$  and  $\mathbf{X}^n$  represents the nodal position vector in the discrete domain of interface in the deformed and undeformed configuration, respectively, the superscript  $n$  denotes nodal quantities, and  $\mathbf{N}$  is defined in the natural parametric space  $\{\xi, \eta\} \in [-1, 1] \times [-1, 1]$ , where  $\xi$  and  $\eta$  are natural coordinates defined in the middle surface of the element. The matrix form of  $\mathbf{N}$  is expressed as

$$\mathbf{N} = [\mathbf{N}_1 \mathbf{1} \quad \mathbf{N}_2 \mathbf{1} \quad \mathbf{N}_3 \mathbf{1} \quad \mathbf{N}_4 \mathbf{1}] \quad (15)$$

where  $\mathbf{1}$  is a  $3 \times 3$  identity matrix, and  $\mathbf{N}_1, \mathbf{N}_2, \mathbf{N}_3$  and  $\mathbf{N}_4$  presents the following expression

$$\mathbf{N}_1 = \frac{1}{4}(1 - \xi)(1 - \eta) \quad (16a)$$

$$\mathbf{N}_2 = \frac{1}{4}(1 + \xi)(1 - \eta) \quad (16b)$$

$$\mathbf{N}_3 = \frac{1}{4}(1 + \xi)(1 + \eta) \quad (16c)$$

$$\mathbf{N}_4 = \frac{1}{4}(1 - \xi)(1 + \eta) \quad (16d)$$

The matrix form of  $\mathbf{M}$  is given as

$$\mathbf{M} = \frac{1}{2} \begin{bmatrix} \mathbf{1} & \mathbf{0} & \mathbf{0} & \mathbf{0} & \mathbf{1} & \mathbf{0} & \mathbf{0} & \mathbf{0} \\ \mathbf{0} & \mathbf{1} & \mathbf{0} & \mathbf{0} & \mathbf{0} & \mathbf{1} & \mathbf{0} & \mathbf{0} \\ \mathbf{0} & \mathbf{0} & \mathbf{1} & \mathbf{0} & \mathbf{0} & \mathbf{0} & \mathbf{1} & \mathbf{0} \\ \mathbf{0} & \mathbf{0} & \mathbf{0} & \mathbf{1} & \mathbf{0} & \mathbf{0} & \mathbf{0} & \mathbf{1} \end{bmatrix} \quad (17)$$

where  $\mathbf{0}$  denotes  $3 \times 3$  null matrix. Similarly, the displacement vector of any material point belonging to the middle surface of the interface domain in the reference configuration  $\bar{\mathbf{u}}^e$  can be calculated through the isoparametric scheme from the nodal vales

$$\bar{\mathbf{u}}^e = \mathbf{N}\mathbf{M}\mathbf{d} \quad (18)$$

where  $\mathbf{d}$  denotes the nodal displacement vector and it is expressed as

$$\mathbf{d} = (u_1, v_1, u_2, v_2, u_3, v_3, u_4, v_4, u_5, v_5, u_6, v_6, u_7, v_7, u_8, v_8)^T \quad (19)$$

In line with derivations proposed for 3D application in [28], the convective shear vector  $\mathbf{s}$ , tangential vector  $\mathbf{t}$  and normal vector  $\mathbf{n}$  to the middle surface in the deformed configuration, see Fig. 3, are defined via the differentiation of average position vector with respect to the natural coordinates  $\xi$  and  $\eta$ , which is expressed as

$$\mathbf{s} = \frac{\partial \bar{\mathbf{x}}^e}{\partial \xi}, \quad \mathbf{t} = \frac{\partial \bar{\mathbf{x}}^e}{\partial \eta}, \quad \mathbf{n} = \mathbf{s} \times \mathbf{t} \quad (20)$$

The gap vector  $\mathbf{g}$  can be determined by multiplying the nodal displacement vector of the interface element with an appropriate operator  $\mathbf{L}$ , which provides the difference between the bottom and upper surface displacements, and its expression is given by

$$\mathbf{g}^e = \mathbf{N}\mathbf{L}\mathbf{d} \quad (21)$$

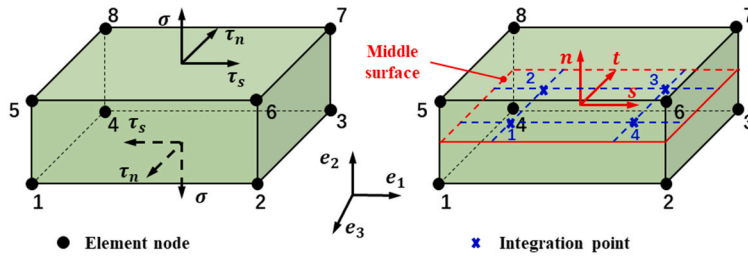


Fig. 3. A sketch of three-dimensional interface element with element nodes and integration points.

where the difference matrix is defined as

$$L = \begin{bmatrix} -1 & 0 & 0 & 0 & 1 & 0 & 0 & 0 \\ 0 & -1 & 0 & 0 & 0 & 1 & 0 & 0 \\ 0 & 0 & -1 & 0 & 0 & 0 & 1 & 0 \\ 0 & 0 & 0 & -1 & 0 & 0 & 0 & 1 \end{bmatrix} \quad (22)$$

In order to distinguish between the different fracture modes, the constitutive relationship between the traction and gap vector of the interface is usually defined in the local frame given by Eq. (8). Therefore, the gap vector in this local frame needs to be computed by multiplying the gap vector in the global frame with a rotation matrix operator

$$g_{loc}^e = Rg^e = RNld \quad (23)$$

The rotation matrix reads

$$R = \begin{bmatrix} s_x & s_y & s_z \\ t_x & t_y & t_z \\ n_x & n_y & n_z \end{bmatrix} \quad (24)$$

where its coefficients are all components of the convective normal and tangential vectors defined in Eq. (20). It is worth noting that this rotation operator is a function of the displacement vector in this large deformation setting. This dependency is subsequently considered in the consistent linearization of the discrete version of interface contribution to the Principle of Virtual Work required by the application of the Newton–Raphson scheme in this study. Note that this dependency on displacements will also lead to a geometrical contribution to the stiffness matrix. Regarding the virtual variation described in Eq. (12), the partial derivative of the local gap vector with respect to nodal displacements is given by

$$\frac{\partial g_{loc}^e}{\partial d} = R(d)NL + \frac{\partial R(d)}{\partial d}NLd \quad (25)$$

where the differentiation of rotation matrix  $R$  with respect to the components of displacement vector  $d$  is a third-order tensor. For convenience, the operator  $B = NL$  is introduced to simplify the above equation as

$$\frac{\partial g_{loc}^e}{\partial d} = R(d)B + \frac{\partial R(d)}{\partial d}Bd \quad (26)$$

Inserting Eq. (26) into Eq. (12) for the virtual variation, where the displacement vector  $u$  is replaced by the nodal vector  $d$ , the following general variational form of interface element considering both geometrical and material nonlinearity is derived as

$$\delta \Pi_{int}^e = \delta d^T \int_{S_0} \left( R(d)B + \frac{\partial R(d)}{\partial d}Bd \right)^T T dS = \delta d^T f_{int}^e \quad (27)$$

where the vector  $\delta d$  represents the kinematically admissible virtual nodal displacement, and  $f_{int}^e$  is a nonlinear function of the nodal displacement vector, which stands for the internal force vector of interface at the element level in the Newton–Raphson incremental-iterative solution scheme. The linearization of for the computation of the incremental correction of the nodal displacements reads

$$K^{e,k} \Delta d^{k+1} = -f_{int}^{e,k} \quad (28a)$$

$$d^{k+1} = d^k + \Delta d^{k+1} \quad (28b)$$

For convenience, and to abbreviate the notation, the superscript  $k$  is omitted in the following. The element stiffness  $K^e = \frac{\partial f_{int}^e}{\partial d}$  is evaluated by the displacement solution field at the iteration  $k$ , which is given by

$$K^e = \int_{S_0} \left[ 2B^T \frac{\partial R^T}{\partial d} T + \left( B^T R^T + d^T B^T \frac{\partial R^T}{\partial d} \right) \frac{\partial T}{\partial d} \right] dS \quad (29)$$

In this formulation, the second derivative of the rotation matrix with respect to the displacement vector that arises for the linearization is omitted for convenience, since it was pointed out in [32] that this term has an almost negligible effect on the

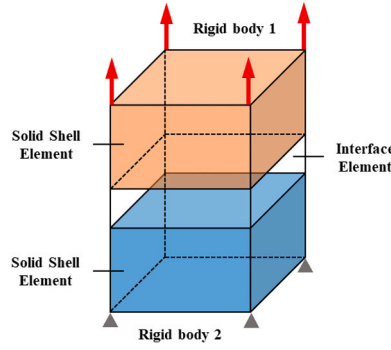


Fig. 4. A sketch of one single element simulation.

simulation results and convergence rate. The derivative of the cohesive traction vector with respect to the nodal displacement vector can be obtained by chain rule as follows,

$$\frac{\partial \mathbf{T}}{\partial \mathbf{d}} = \frac{\partial \mathbf{T}}{\partial \mathbf{g}_{\text{loc}}} \frac{\partial \mathbf{g}_{\text{loc}}}{\partial \mathbf{d}} = \mathbf{C}\mathbf{R}(\mathbf{d})\mathbf{B} + \frac{\partial \mathbf{R}(\mathbf{d})}{\partial \mathbf{d}}\mathbf{B}\mathbf{d} \quad (30)$$

where the tangent material stiffness matrix  $\mathbf{C} = \frac{\partial \mathbf{T}}{\partial \mathbf{g}_{\text{loc}}}$  has been given in Sec. 2. Substituting Eq. (30) into Eq. (29), we can get the following element stiffness matrix as

$$\mathbf{K}^e = \mathbf{K}_{\text{mat}}^e + \mathbf{K}_{\text{geom}}^e \quad (31a)$$

$$\mathbf{K}_{\text{mat}}^e = \int_{S_0} \mathbf{B}^T \mathbf{R}^T \mathbf{C} \mathbf{R} \mathbf{B} \, dS \quad (31b)$$

$$\mathbf{K}_{\text{geom}}^e = \int_{S_0} \left[ 2\mathbf{B}^T \frac{\partial \mathbf{R}^T}{\partial \mathbf{d}} \mathbf{T} + \mathbf{d}^T \mathbf{B}^T \frac{\partial \mathbf{R}^T}{\partial \mathbf{d}} \mathbf{C} \frac{\partial \mathbf{R}}{\partial \mathbf{d}} \mathbf{B} \mathbf{d} + \left( \mathbf{B}^T \mathbf{R}^T \mathbf{C} \frac{\partial \mathbf{R}}{\partial \mathbf{d}} \mathbf{B} \mathbf{d} + \mathbf{d}^T \mathbf{B}^T \frac{\partial \mathbf{R}^T}{\partial \mathbf{d}} \mathbf{C} \mathbf{R} \mathbf{B} \right) \right] dS \quad (31c)$$

where  $\mathbf{K}_{\text{geom}}^e$  and  $\mathbf{K}_{\text{mat}}^e$  are the element geometrical stiffness matrix and the material stiffness matrix, respectively. In small displacement, the element stiffness reduces to the material stiffness contribution only, while in large displacement, the geometrical stiffness term also needs to be considered for the sake of accuracy. The present formulation has been implemented as a user element UEL in the finite element software ABAQUS.

#### 4. Verification and application to recycling of photovoltaics

In this section, the coupled CZM in the three-dimensional interface element framework is firstly validated by comparing the numerical results with the experimental results in [14], and then difference between the specific energy required for peeling and crushing of a PV module is quantified to underline the potential application of the proposed modeling approach to design novel methods for PV recycling.

##### 4.1. Benchmark test

To better illustrate the constitutive behavior of polynomial CZM and the performance of the 3D interface finite element, a benchmark simulation with one single element under uniaxial tension is performed, see the sketch in Fig. 4. The upper and lower bodies are both modeled using solid shell elements with rigid material properties, while the middle ply is modeled with the present large deformation interface finite element. The bottom surface of the lower body is constrained in the loading direction, and its reaction force is computed as the peeling force. Traction stress is calculated from the reaction force divided by the interface area. In the simulation, the maximum stress of the polynomial CZM is kept with the constant value of 0.3 MPa. The predicted traction vs. separation curves with different ultimate displacements ranging from 1 mm to 15 mm are shown in Fig. 5. The simulation results clearly demonstrate the generalized characteristics of the polynomial CZM incorporated into the 3D large deformation interface finite element. It can be seen that the stiffness of the traction-separation curves before the peak traction decreases with an increased ultimate displacement value. For each case, the resultant curve presents a softening stage when traction reaches the maximum value 0.3 MPa, and complete separation occurs at the corresponding ultimate displacement.

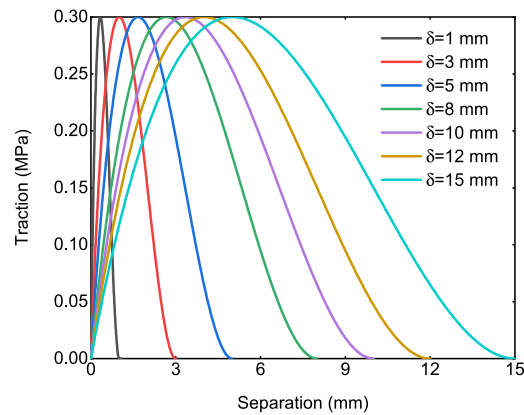


Fig. 5. Traction separation curves of one single element simulation with different ultimate displacement values.

**Table 1**

Testing conditions for Photovoltaic modules.

T(°C)	RH		
	85%	65%	45%
95	√		
85	√	√	√
65	√		

**Table 2**

Mechanical properties for Photovoltaic modules [40,41].

	E (GPa)	Density (kg/m <sup>3</sup> )
Backsheet	2.8	1200
EVA	0.01	1180
Glass	73	2500

#### 4.2. FE simulation and parameters identification

In the following, the large deformation interface finite element and the polynomial CZM equipped with the humidity dose model are applied for the simulation of the experimental work reported in [14]. This application is chosen in order to prove the validity of the proposed modeling framework. In the experimental study aforementioned, the degradation of adhesion strength between the backsheet and encapsulant layers at different humidity and temperature levels after a certain time interval was investigated in detail. The encapsulant material is EVA with a thickness of 0.4 mm, and the backsheet is composed of two layers of PolyEthylene Terephthalate (PET) with a total thickness of 0.25 mm. Laminates were cut by CO<sub>2</sub> laser into the peel strips with a width of 10 mm and length of 100 mm for each one, see Fig. 6(a). The first 15 mm length of each specimen was peeled off before the test to form a tap that can be held by the grip of the testing machine. Controlled 90-degree peeling tests were performed in the environmental chambers to obtain the adhesion strength during exposure to the damp-heat conditions. The loading speed was 50 mm/min for each test. The indoor accelerated tests were performed at five different temperature and humidity conditions, as listed in Table 1.

For the numerical simulation as shown in Fig. 6(b), the upper backsheet ply and lower ply are modeled using the 8-node solid shell elements in which both the enhanced assumed strain method [36,37] and the assumed natural strain method [38,39] are adopted in order to alleviate locking phenomena according to the state-of-the-art in this field. Since the elastic material properties of the backsheet are not given in [14], the values corresponding to the standard materials in the PV system [40,41] are adopted in this study, see Table 2. Young's modulus of the backsheet is 2.8 GPa, and Poisson's ratio is set to 0.2. The mechanical properties for the lower layer are selected coinciding with those corresponding to glass properties, with: Poisson ratio equal to zero and Young's modulus equal to 73 GPa. Another uncertainty comes from how peeling extension was measured since it was not clearly pointed out in the experimental study. In the simulation, vertical displacement at the upper crack edge position (see Fig. 6(b)) is adopted for its measurement. The size of the solid shell finite elements for modeling the substrate layers is 1 mm, and the total number of solid shell finite elements is 2000 for the whole model. The middle ply with a thickness of 0.2 mm is herein modeled as a cohesive interface using the large deformation interface finite elements above. A total of 850 interface finite elements is present in the model. All the nodal degrees of freedom at the bottom surface are constrained, and vertical displacement boundary conditions are applied at the tip end of the laminate to peel off the upper backsheet. Reaction forces at all their constrained nodes add up to compute the peeling force.

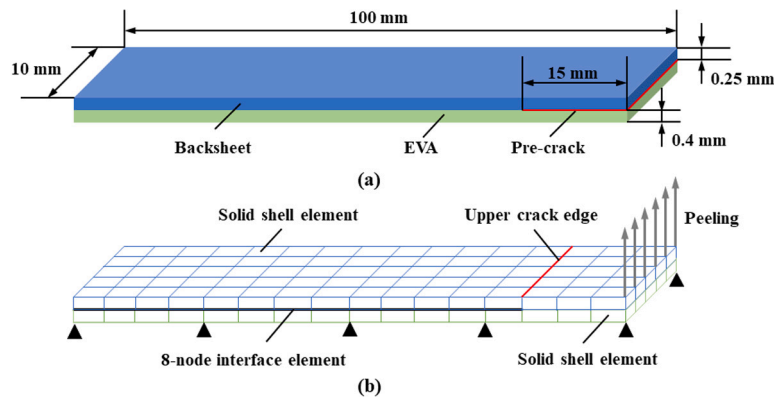


Fig. 6. (a) 90-degree peeling test, and (b) discretization.

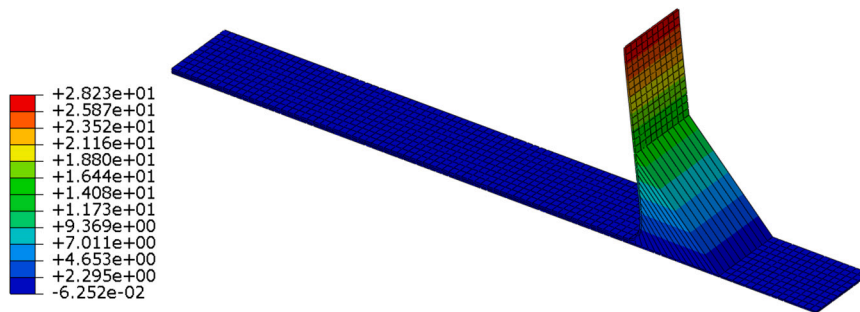


Fig. 7. Displacement contour in the peeling direction along the simulation process.

### 4.3. Numerical results and verification

The displacement contour plot for the finite element model under large deformation for peeling simulation is shown in Fig. 7. Simulation results regarding peeling force vs. vertical displacement of fictitious extension tip for different exposure duration at the same condition 85 °C/85% RH are plotted in Fig. 8(a). In these simulations, the only variable parameter is the exposure duration, while all the other conditions are kept constant to investigate the effect of exposure on the adhesion degradation. All four curves for different exposure duration show a similar pattern. The peeling force increases gradually from the beginning of the peeling process as the loading displacement boundary condition is applied to the specimen, and when the gaps of crack tip reach the ultimate displacement value set in the cohesive zone model, debonding occurs in these elements and the overall response shows a plateau evolution during the subsequent crack propagation process.

In the experimental study [14], it was pointed out that testing curves for peeling present inescapable differences even for the same batch of specimen due to the imperfect lamination quality and variation of the manufacturing process of materials. Therefore, the obtained experimental data of adhesion strength were computed as an average value of the different tests at a certain exposure and simulated accelerated environmental condition. For calculation of numerical values, the resultant simulation curve is firstly integrated from the starting of debonding to the end. Then the adhesion strength can be obtained by dividing that value by the corresponding range. Comparison between experimental and numerical adhesion strength values for different exposure at a certain hygrothermal condition corresponding to 85 °C/85% RH is shown in Fig. 8(b). It is clearly demonstrated that exposure time significantly impacts PV interfacial adhesion as the strength of 22.81 N/cm degrades to 5.64 N/cm after exposure to the damp-heat condition for 72 h. For the exposure duration of 0 h, 24 h, 48 h, and 72 h, numerical results correlate with individual experimental results very well, as shown in Fig. 8(b).

Peeling force vs. vertical extension displacement curves for different relative humidity conditions obtained from finite element simulation are shown in Fig. 9(a). The temperature and exposure time are kept constant in this case, and set as 85 °C and 72 h, respectively. The curves show the different plateau values of the peeling force for the three different conditions. Higher relative humidity at the same temperature and exposure condition leads to an increased degradation of adhesion strength. A comparison of adhesion strength at different humidity levels between experiment and simulation is shown in Fig. 9(b). Current predictions exhibit a satisfactory agreement with respect to available experimental results for any RH level.

Resultant curves for different temperature values at the condition of 85% RH with exposure time of 72 h are shown in Fig. 10(a). As mentioned before, temperature is regarded as the accelerating factor of humidity that indirectly affects the adhesion strength.

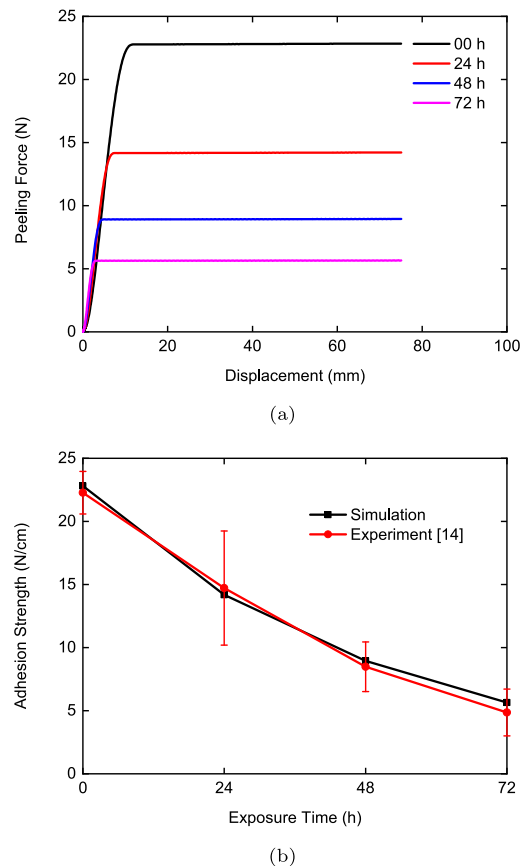


Fig. 8. (a) Peeling force vs. displacement curves obtained from simulation (b) Comparison of adhesion strength between experiment and simulation with different exposure duration at the same condition 85 °C/85% RH.

The high-temperature condition would result in significant adhesion degradation in the PV system. As shown in Fig. 10(b), adhesion strength decreases from 15.17 N/cm to 1.93 N/cm when the temperature increases from 65 °C to 95 °C. The numerical prediction matches the experimental results very well with slight difference for all the three considered cases. It should be pointed out that adhesion strength between different plies in PV laminate is affected by many additional complex failure mechanisms in the outdoor environment, and the comprehensive degradation model would require further work. This study mainly focuses on a reliable modeling method of the effect of steady humidity and temperature conditions following the experimental work [14]. In addition to the variation of same batch specimens, there are some other inevitable experimental error sources due to other failure mechanisms triggered during testing. Taking these into account, the difference between simulation and experiment can be considered as acceptable from an engineering standpoint.

In order to further assess the modeling strategy proposed in this study, all the numerical results obtained for different humidity, temperature, and exposure time conditions are compared with experimental results in terms of adhesion strength versus humidity dose values, as shown in Fig. 11. The experimental curve is obtained by curve fitting with all the experimental results reported in [14]. As mentioned in Section 2, humidity dose is introduced to provide a groundwork insight into the hygrothermal effect on adhesion, and it is defined in Eq. (4). This definition allows assessing the unified environmental influence under different relative humidity and temperature conditions. It can be seen that the predictions of adhesion strength show an exponential decay with respect to humidity dose values and also perfectly agree with the experimental fitting curve.

#### 4.4. Technical application to recycling of PV modules

Although a PV system can produce green power for 25–30 years during its service phase, the total environmental impact should be assessed throughout its entire lifetime. Much attention has been paid to the environmentally friendly manufacturing of PV modules nowadays, but efforts specifically focused on the treatment of end-of-life products are still limited. Recycling can not only effectively prevent the toxic and hazardous substances in PV products from entering the groundwater and soil, and thus causing negative biochemical effects on the environment [42,43], but also conserves precious metal materials such as Silver, Germanium, Cadmium, etc. and energy-intensive pure material such as Silicon wafer [44]. In general, recycling of end-of-life PV products can significantly

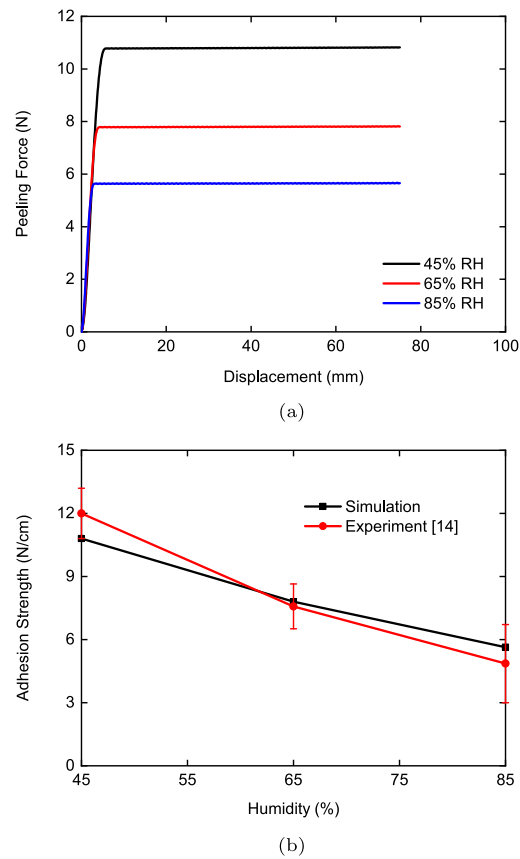
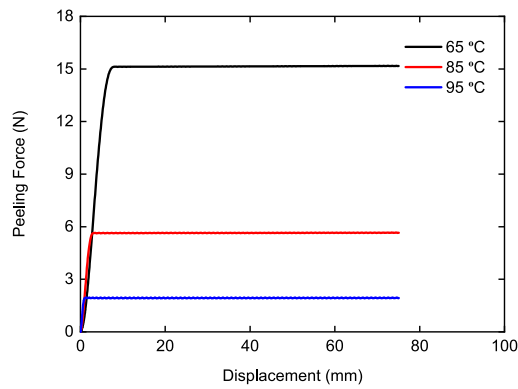


Fig. 9. (a) Peeling force vs. displacement curves obtained from simulation (b) Comparison of adhesion strength between experiment and simulation for different relative humidity values at the same condition 85 °C and exposure duration of 72 h.

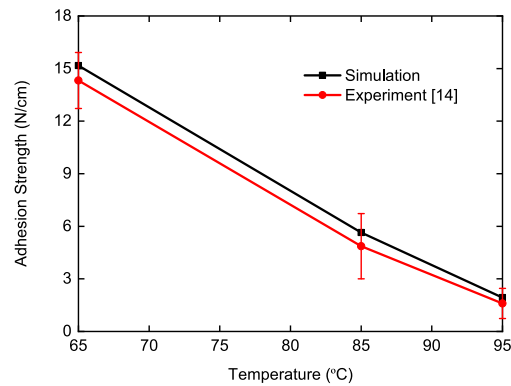
reduce carbon emission and global energy consumption, and alleviate lifecycle depletion of Silicon as well [45], which helps meet the growing demand of this raw material in PV industry. Despite these benefits, it is very difficult for recycling to be widely recognized without taking the economic factor into account. In this concern, previous studies [43,46] have shown that recycling Silicon PV modules lacks economic sustainability due to high energy consumption of the largely adopted recycling processes. Following the removal of external Aluminum frame and junction box of end-of-life PV products for recycling, the remainder of PV panel is usually subjected to the industrial crushing process including blade rotor crushing without any controlling sieve and hammer crushing with controlling sieve [47], which would inevitably consume a lot of energy [48] and thus increase the recycling cost. An innovative idea is to explore the present modeling approach to virtually assess the efficacy of a different way to disassemble PV modules by peeling of the set of bonded laminae from the glass cover, to completely circumvent the crushing step.

The histogram of peeling energy per unit mass of testing specimen for different temperature and relative humidity conditions is shown in Fig. 12. At the same relative humidity, the specific energy required for peeling at a high temperature condition is much lower than that at a low temperature condition. At 85% RH, the maximum peeling energy in the 65 °C condition is equal to 1.572 J/g, which is approximately eight times the energy value of 0.2 J/g required for the 95 °C condition. Conclusion can be drawn that end-of-life PV modules installed in high temperature areas are much easier to be recycled by the peeling method compared to those installed in cold areas, since adhesion degradation is accelerated by temperature as mentioned before. Besides, it is also noted that moisture has the same effect as temperature on the required specific energy. Less energy would be required under increased relative humidity or moisture to peel off the different plies of PV laminate for recycling. At the temperature conditions of 85 °C, the peeling energy in 45% RH is 1.12 J/g, while in 85% RH condition, only specific energy value of 0.584 J/g is required as high relative humidity causes more severe adhesion degradation in PV, which means end-of-life PV installed in hot-humid areas should be more easily recycled through peeling. It should be pointed out that standard qualification tests to assess the constant temperature and moisture effect on the adhesion of PV is carried out in the 85 °C and 85% RH condition. Different specific peeling energy values for different exposure times 0 h, 24 h, 48 h and 72 h at this condition are listed in Fig. 12. It is clear that PV modules subjected to the hygrothermal degradation are prone to be recycled by peeling as compared to brand new products, since longer exposure times leads to less required specific peeling energy, as can be seen from the standard damp-heat condition of 85 °C and 85% RH.

With the aim of highlighting the tremendous advantage of exploring peeling method for recycling over conventional crushing strategy, the tentative analysis and comparison between these two methods are discussed here. Relationship of average particle size



(a)



(b)

Fig. 10. (a) Peeling force vs. displacement curves obtained from simulation (b) Comparison of adhesion strength between experiment and simulation for different temperature values at the same condition 85% RH and exposure duration of 72 h.

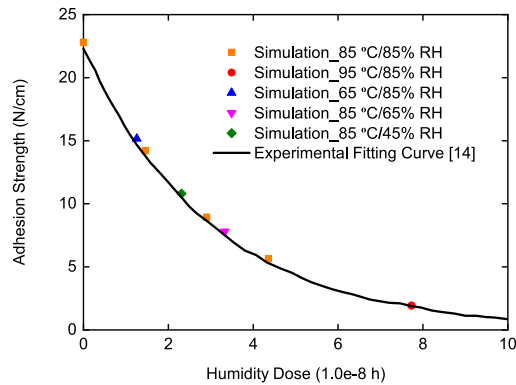


Fig. 11. Comparison of adhesion strength versus humidity dose for different conditions between experimental fitting and numerical results.

with required crushing energy per unit mass of PV modules reported in [49] is shown in Fig. 13. The basic trend is that particles during the crushing process of end-of-life PV modules concentrate on smaller size fraction with the increased energy. In [49], various models were adopted to fit the experimental results, and it was concluded that Walker’s model is the best one to describe the relationship between particle size and specific energy required for recycling by crushing and fragmentation of PV modules. From this fitting curve and experimental results shown in Fig. 13, it can be evaluated that the input energy to dismantle the PV panel into 5 mm particles for subsequent recycling is approximately 180 J/g, which is more than hundred time the estimated specific energy required by peeling. Therefore, it can be concluded that recycling by peeling should be a much more economically promising method as compared to crushing, due to the extremely low energy consumption. The modeling framework proposed in this work can be

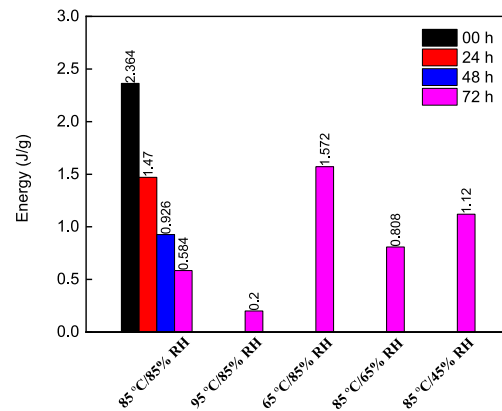


Fig. 12. Comparison of the required specific energy for different relative humidity and temperature conditions.

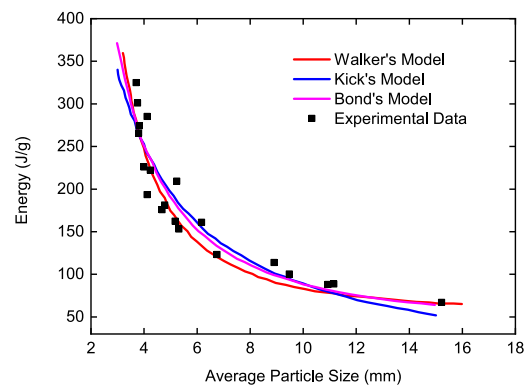


Fig. 13. Relationship of average particle size with the required specific energy for crushing in recycling of PV [49].

very advantageous to explore new peeling setups and environmental conditioning of PV modules using accelerated ageing tests to optimize disassembling operations and replace crushing for recycling end-of-life PV panels in the foreseeable future.

## 5. Conclusions

In order to investigate the adhesion degradation of PV laminates due to humidity ingress and temperature effects, a modeling framework coupling the cohesive zone model with a humidity dose model has been proposed in this study. A 3D interface finite element considering large deformation including both geometrical and material nonlinearities is also established to accurately simulate the interfacial failure in the 90-degree peeling test. The corresponding FE implementation is based on the variational form of interface contribution to the Principle of Virtual Work of the whole mechanical system, and its subsequent consistent linearization considering large deformation is also detailed. To validate the modeling strategy, peeling between the backsheets and the encapsulant layer (EVA) has been simulated to assess the adhesion strength at different hygrothermal environments after certain exposure duration. Numerical results have been compared with experimental results [14] under different conditions of exposure time, humidity and temperature, and they correlate with damp-heat test results very well. All the predicted adhesion strength values show exactly the same exponential decay trend as the experimental one. With the aid of this modeling framework, considering large deformation and coupling of both temperature and humidity, a realistic numerical simulation of peeling for recycling of end-of-life PV panels is possible. Compared with the traditional crushing in PV recycling process, it has been assessed that the specific required energy for peeling is much lower, which indicates that the modeling framework proposed in this work can be very valuable for PV industry to virtually explore new economical solutions for recycling.

It should be concluded that though adhesion strength, which is greatly affected by environmental moisture and temperature, is of utmost significance to the durability and performance of PV modules, no suitable modeling method within the large deformation framework addressed these factors before. However, the proposed modeling method for virtual testing can be highly beneficial to the PV industry. For instance, it can be used to virtually simulate the peeling of the different plies of end-of-life PV laminates for recycling under different degradation levels, so as to estimate how much energy it would be required. Such a computational tool would be beneficial since both large deformation and degradation due to hygrothermal effects are taken into account.

This work represents the first step to model the peeling behavior of interfaces in PV systems subject to steady hygrothermal conditions. In order to model realistic outdoor environments for PV, including not only the effect of constant humidity and temperature but also varying humidity and cyclic temperature variations over time, further research is needed. Additional collaborative experimental and numerical efforts are therefore required to predict adhesion degradation in PV systems over time in different relevant climate zones where PV modules are installed.

### Declaration of competing interest

The authors declare that they have no known competing financial interests or personal relationships that could have appeared to influence the work reported in this paper.

### Acknowledgments

The authors acknowledge funding received from the European Union's H2020-MSCA-ITN-2019 research and innovation program under the Marie Skłodowska-Curie grant agreement no. 861061 – Project NEWFRAC "New strategies for multifield fracture problems across scales in heterogeneous systems for Energy, Health and Transport".

JR is grateful to the Consejería de Economía y Conocimiento of the Junta de Andalucía (Spain) for financial support under the contract US-1265577-Programa Operativo FEDER Andalucía 2014-2020, and the support of the Spanish Ministerio de Ciencia, Innovación y Universidades the under the grant PID2019-109723GB-I00 and Consejería de Economía y Conocimiento of the Junta de Andalucía (Spain) under the grant P2-00595.

### References

- [1] Polverini D, Field M, Dunlop E, Zaaïman W. Polycrystalline silicon PV modules performance and degradation over 20 years. *Prog Photovolt, Res Appl* 2013;21(5):1004–15.
- [2] Deng G, Ma W, Peng Y, Wang S, Yao S, Peng S. Experimental study on laminated glass responses of high-speed trains subject to windblown sand particles loading. *Constr Build Mater* 2021;300:124332.
- [3] McIntosh KR, Powell NE, Norris AW, Cotsell JN, Ketola BM. The effect of damp-heat and UV aging tests on the optical properties of silicone and EVA encapsulants. *Prog Photovolt, Res Appl* 2011;19(3):294–300.
- [4] Schneller E, Shiradkar NS, Dhare NG. Performance variation of commercially available modules after six months of outdoor system voltage stress testing. In: 2014 IEEE 40th photovoltaic specialist conference. IEEE; 2014, p. 3216–9.
- [5] de Oliveira MCC, Cassini DA, Diniz ASAC, Soares LG, Viana MM, Kazmerski LL, et al. Comparison and analysis of performance and degradation differences of crystalline-Si photovoltaic modules after 15-years of field operation. *Sol Energy* 2019;191:235–50.
- [6] Omazic A, Oreski G, Halwachs M, Eder G, Hirschl C, Neumaier L, et al. Relation between degradation of polymeric components in crystalline silicon PV module and climatic conditions: A literature review. *Sol Energy Mater Sol Cells* 2019;192:123–33.
- [7] de Oliveira MCC, Cardoso ASAD, Viana MM, Lins VdFC. The causes and effects of degradation of encapsulant ethylene vinyl acetate copolymer (EVA) in crystalline silicon photovoltaic modules: A review. *Renew Sustain Energy Rev* 2018;81:2299–317.
- [8] Quintana M, King D, McMahon T, Osterwald C. Commonly observed degradation in field-aged photovoltaic modules. In: Conference record of the twenty-ninth IEEE photovoltaic specialists conference, 2002. IEEE; 2002, p. 1436–9.
- [9] Dadaniya A, Datla NV. Degradation prediction of encapsulant-glass adhesion in the photovoltaic module under outdoor and accelerated exposures. *Sol Energy* 2020;208:419–29.
- [10] Dhare NG, Kaul A, Pethe SA, Schneller E, Shiradkar NS. Outdoor performance testing of thin-film PV modules in the hot and humid climate. In: 2013 IEEE 39th photovoltaic specialists conference. IEEE; 2013, p. 2994–7.
- [11] Kempe M. Overview of scientific issues involved in selection of polymers for pv applications. In: 2011 37th IEEE photovoltaic specialists conference. IEEE; 2011, 000085–000090.
- [12] Svorčík V, Ekrt O, Rybka V, Lipták J, Hnatowicz V. Permittivity of polyethylene and polyethyleneterephthalate. *J Mater Sci Lett* 2000;19(20):1843–5.
- [13] Ferguson TP, Qu J. An engineering model for moisture degradation of polymer/metal interfacial fracture toughness. In: Proceedings. international symposium on advanced packaging materials: processes, properties and interfaces, 2005. IEEE; 2005, p. 298–301.
- [14] Wu D, Zhu J, Betts TR, Gottschalg R. Degradation of interfacial adhesion strength within photovoltaic mini-modules during damp-heat exposure. *Prog Photovolt, Res Appl* 2014;22(7):796–809.
- [15] Datla N, Ameli A, Azari S, Papini M, Spelt J. Effects of hygrothermal aging on the fatigue behavior of two toughened epoxy adhesives. *Eng Fract Mech* 2012;79:61–77.
- [16] Liu Z, Xia Y, Guo S. Characterization methods of delamination in a plain woven CFRP composite. *J Mater Sci* 2019;54(20):13157–74.
- [17] Krueger R. Virtual crack closure technique: History, approach, and applications. *Appl Mech Rev* 2004;57(2):109–43.
- [18] Hillerborg A. Fracture mechanics concepts applied to moment capacity and rotational capacity of reinforced concrete beams. *Eng Fract Mech* 1990;35(1–3):233–40.
- [19] Carpinteri A. Finite deformation effects in homogeneous and interfacial fracture. *Eng Fract Mech* 1989;32:265–78.
- [20] Carpinteri A. Cusp catastrophe interpretation of fracture instability. *J Mech Phys Solids* 1989;37(5):567–82.
- [21] Carpinteri A. Softening and snap-back instability in cohesive solids. *Internat J Numer Methods Engrg* 1989;28(7):1521–37.
- [22] Reinoso J, Blázquez A, Estefani A, París F, Cañas J, Arévalo E, et al. Experimental and three-dimensional global-local finite element analysis of a composite component including degradation process at the interfaces. *Composites B* 2012;43(4):1929–42.
- [23] Liu Z, Xia Y. Development of a numerical material model for axial crushing mechanical characterization of woven CFRP composites. *Compos Struct* 2019;230:111531.
- [24] Massabò R, Darban H. Mode II dominant fracture of layered composite beams and wide-plates: a homogenized structural approach. *Eng Fract Mech* 2019;213:280–301.
- [25] Paggi M, Wriggers P. A nonlocal cohesive zone model for finite thickness interfaces—Part I: mathematical formulation and validation with molecular dynamics. *Comput Mater Sci* 2011;50(5):1625–33.
- [26] Paggi M, Lehmann E, Weber C, Carpinteri A, Wriggers P, Schaper M. A numerical investigation of the interplay between cohesive cracking and plasticity in polycrystalline materials. *Comput Mater Sci* 2013;77:81–92.
- [27] Paggi M, Wriggers P. Stiffness and strength of hierarchical polycrystalline materials with imperfect interfaces. *J Mech Phys Solids* 2012;60(4):557–72.

- [28] Paggi M, Reinoso J. An anisotropic large displacement cohesive zone model for fibrillar and crazing interfaces. *Int J Solids Struct* 2015;69:106–20.
- [29] Ortiz M, Pandolfi A. Finite-deformation irreversible cohesive elements for three-dimensional crack-propagation analysis. *Internat J Numer Methods Engrg* 1999;44(9):1267–82.
- [30] Roychowdhury S, Roy YDA, Dodds Jr RH. Ductile tearing in thin aluminum panels: experiments and analyses using large-displacement, 3-D surface cohesive elements. *Eng Fract Mech* 2002;69(8):983–1002.
- [31] van den Bosch M, Schreurs P, Geers M. A cohesive zone model with a large displacement formulation accounting for interfacial fibrillation. *Eur J Mech A Solids* 2007;26(1):1–19.
- [32] Reinoso J, Paggi M. A consistent interface element formulation for geometrical and material nonlinearities. *Comput Mech* 2014;54(6):1569–81.
- [33] Tvergaard V. Effect of fibre debonding in a whisker-reinforced metal. *Mater Sci Eng A* 1990;125(2):203–13.
- [34] Koehl M, Heck M, Wiesmeier S. Modelling of conditions for accelerated lifetime testing of humidity impact on PV-modules based on monitoring of climatic data. *Sol Energy Mater Sol Cells* 2012;99:282–91.
- [35] Lam DCC, Yang F, Tong P. Chemical kinetic model of interfacial degradation of adhesive joints. *IEEE Trans Compon Packag Technol* 1999;22(2):215–20.
- [36] Bischoff M, Ramm E. Shear deformable shell elements for large strains and rotations. *Internat J Numer Methods Engrg* 1997;40(23):4427–49.
- [37] Klinkel S, Wagner W. A geometrical non-linear brick element based on the EAS-method. *Internat J Numer Methods Engrg* 1997;40(24):4529–45.
- [38] Dvorkin E, Bathe K. A continuum mechanics based four-node shell element for general non-linear analysis. *Eng Comput* 1984;1(1):77–88.
- [39] Betsch P, Stein E. An assumed strain approach avoiding artificial thickness straining for a non-linear 4-node shell element. *Commun Numer Methods Eng* 1995;11(11):899–909.
- [40] Paggi M, Kajari-Schröder S, Eitner U. Thermomechanical deformations in photovoltaic laminates. *J Strain Anal Eng Des* 2011;46(8):772–82.
- [41] Corrado M, Infuso A, Paggi M. Simulated hail impacts on flexible photovoltaic laminates: testing and modelling. *Meccanica* 2017;52(6):1425–39.
- [42] Tao J, Yu S. Review on feasible recycling pathways and technologies of solar photovoltaic modules. *Sol Energy Mater Sol Cells* 2015;141:108–24.
- [43] D'Adamo I, Miliacca M, Rosa P. Economic feasibility for recycling of waste crystalline silicon photovoltaic modules. *Int J Photoenergy* 2017;2017.
- [44] Goe M, Gaustad G. Strengthening the case for recycling photovoltaics: An energy payback analysis. *Appl Energy* 2014;120:41–8.
- [45] Huang B, Zhao J, Chai J, Xue B, Zhao F, Wang X. Environmental influence assessment of China's multi-crystalline silicon (multi-Si) photovoltaic modules considering recycling process. *Sol Energy* 2017;143:132–41.
- [46] Cucchiella F, Rosa P, et al. End-of-life of used photovoltaic modules: A financial analysis. *Renew Sustain Energy Rev* 2015;47:552–61.
- [47] Granata G, Pagnanelli F, Moscardini E, Havlik T, Toro L. Recycling of photovoltaic panels by physical operations. *Sol Energy Mater Sol Cells* 2014;123:239–48.
- [48] Liu Z, Xia Y. Numerical and experimental investigation on mechanical responses of plain woven CFRP composite under various loading cases. *Int J Crashworthiness* 2021;26(1):65–76.
- [49] Song B-P, Zhang M-Y, Fan Y, Jiang L, Kang J, Gou T-T, et al. Recycling experimental investigation on end of life photovoltaic panels by application of high voltage fragmentation. *Waste Manage* 2020;101:180–7.